

SHARP: Spectrum-aware Highly-dynamic Adaptation for Resolution Promotion in Remote Sensing Synthesis

Bingxuan Zhao, Qing Zhou, Chuang Yang, and Qi Wang, *Senior Member, IEEE*

Abstract—Text-to-image generation powered by Diffusion Transformers (DiTs) has made remarkable strides, yet remote sensing (RS) synthesis lags behind due to two barriers: the absence of a domain-specialized DiT prior and the prohibitive cost of training at the large resolutions that RS applications demand. Training-free resolution promotion via Rotary Position Embedding (RoPE) rescaling offers a practical remedy, but every existing method applies a *static* positional scaling rule throughout the denoising process. This uniform compression is particularly harmful for RS imagery, whose substantially denser medium- and high-frequency energy encodes the fine structures critical for aerial-scene realism, such as vehicles, building contours, and road markings. Addressing both challenges requires a domain-specialized generative prior coupled with a denoising-aware positional adaptation strategy. To this end, we fine-tune FLUX on over 100,000 curated RS images to build a strong domain prior (RS-FLUX), and propose Spectrum-aware Highly-dynamic Adaptation for Resolution Promotion (SHARP), a training-free method that introduces a rational fractional time schedule $\kappa_{r,s}(t)$ into RoPE. SHARP applies strong positional promotion during the early layout-formation stage and progressively relaxes it during detail recovery, aligning extrapolation strength with the frequency-progressive nature of diffusion denoising. Its resolution-agnostic formulation further enables robust multi-scale generation from a single set of hyperparameters. Extensive experiments across six square and rectangular resolutions show that SHARP consistently outperforms all training-free baselines on CLIP Score, Aesthetic Score, and HPSv2, with widening margins at more aggressive extrapolation factors and negligible computational overhead. Code and weights are available at <https://github.com/bxuanz/SHARP>.

Index Terms—Remote sensing, text-to-image generation, diffusion transformer, rotary position embedding, training-free resolution promotion

I. INTRODUCTION

Remote sensing (RS) imagery plays an indispensable role in Earth observation, supporting applications ranging from urban planning and environmental monitoring to disaster assessment and precision agriculture. The ability to synthesize photo-realistic RS images from textual descriptions would unlock new possibilities for data augmentation, scenario simulation, and training of downstream perception models. Text-to-image

Bingxuan Zhao is with the School of Computer Science and Engineering, and also with the School of Artificial Intelligence, Optics and ElectroNics (iOPEN), Northwestern Polytechnical University, Xi'an 710072, China.

Qing Zhou, Chuang Yang, and Qi Wang are with the School of Artificial Intelligence, Optics and ElectroNics (iOPEN), Northwestern Polytechnical University, Xi'an 710072, China.

Corresponding author: Qi Wang.

E-mail: bxuanzhao202@gmail.com, omtcyang@gmail.com, chautsing@gmail.com, crabwq@gmail.com.

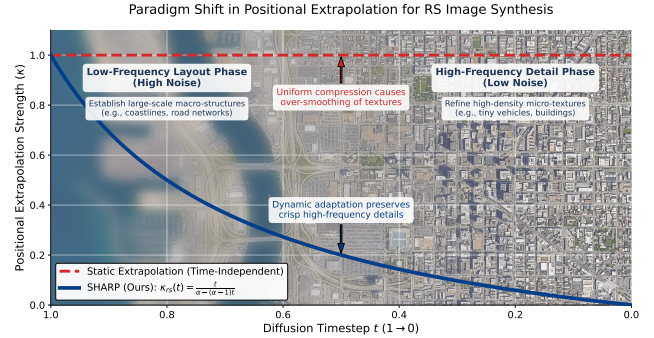


Fig. 1. **Paradigm shift in positional extrapolation for large-scale RS synthesis.** Diffusion-based image generation follows a frequency-progressive paradigm: global layouts emerge at high noise levels, while dense high-frequency details (e.g., vehicles, urban textures) crystallize at low noise levels. Static methods (red dashed) apply uniform extrapolation strength, suppressing the spatial spectrum and causing over-smoothing. **SHARP** (blue solid) introduces a dynamic rational schedule $\kappa_{r,s}(t)$ that aligns extrapolation strength with the denoising progression, preserving crisp high-frequency details without sacrificing structural coherence.

generation powered by Diffusion Transformers (DiTs) [1] has achieved remarkable progress in natural-image synthesis, producing highly realistic and semantically coherent outputs. However, RS text-to-image generation remains significantly underdeveloped compared with its natural-image counterpart.

The gap is rooted in the scope of existing RS generative studies. Most prior work targets conditional tasks such as super-resolution [2], image translation [3], cloud removal [4], and layout-guided synthesis [5, 6] guidance rather than generating from text alone. While these methods have demonstrated the value of generative priors for Earth observation, none of them provide a general-purpose text-to-image foundation model for aerial scenes. Although recent diffusion-based approaches [7, 8] have improved RS generation fidelity, most are designed for patch-level synthesis or conditional restoration. This leaves large-scale RS text-to-image generation without a strong, domain-specialized DiT prior.

The demand for large-scale generation is particularly acute in RS, where a single image must span a broad spatial extent while preserving fine local structures. Compared with natural images, RS imagery exhibits much denser high-frequency content, including vehicles, roof boundaries, road markings, and repetitive urban patterns [9, 10], making faithful synthesis at large scales significantly harder. Directly training DiTs at large resolutions is prohibitively expensive because self-attention cost scales quadratically with the token count, and curating sufficient high-resolution RS training data is itself a

formidable challenge.

Training-free resolution promotion based on Rotary Position Embedding (RoPE) [11] offers a practical alternative: by rescaling positional frequencies at inference time, a pretrained low-resolution model can operate at larger sizes without retraining. Representative approaches include Position Interpolation (PI) [12], NTK-aware scaling [13], and YaRN [14]. Originally developed for extending context windows in large language models, these methods have been adapted for image generation by adjusting positional frequencies in DiTs. However, all of them apply a *static* scaling rule that remains fixed throughout the denoising process.

This static assumption is particularly problematic for RS imagery. Diffusion-based generation follows a frequency-progressive paradigm [15, 16]: early high-noise steps establish global layout, whereas late low-noise steps recover high-frequency details. Static scaling compresses the positional spectrum uniformly at every denoising step, ignoring this temporal structure. For RS images, which carry significantly stronger medium- and high-frequency energy than natural images, the uniform compression suppresses the very frequencies essential for sharp textures and fine structures, producing over-smoothed outputs that lack the geometric precision required for realistic aerial scenes (Fig. 1).

Motivated by this analysis, we propose **Spectrum-aware Highly-dynamic Adaptation for Resolution Promotion (SHARP)** for large-scale RS text-to-image synthesis. Addressing both the domain-prior gap and the positional-extrapolation challenge, our framework operates in two steps: (i) fine-tuning FLUX [17] on over 100,000 curated RS images to build a domain-specialized prior (**RS-FLUX**), and (ii) applying a dynamic RoPE adaptation strategy driven by a rational fractional time schedule $\kappa_{rs}(t)$ that applies strong promotion in the early layout-formation stage and progressively relaxes it in the detail-recovery stage. This design ensures that large-scale spatial organization is maintained without sacrificing the native high-frequency content critical for RS realism, and its resolution-agnostic formulation enables robust multi-scale generation from a single set of hyperparameters. The main contributions are:

- We construct an RS text-to-image corpus of 102,952 prompt-image pairs and fine-tune FLUX as a domain-specialized DiT model, providing a strong foundation for RS text-to-image generation.
- We provide both empirical spectral evidence and analytical derivation showing that static RoPE extrapolation is inconsistent with the frequency-progressive nature of diffusion denoising, with RS imagery being especially susceptible due to its characteristically strong high-frequency energy.
- We propose SHARP, a spectrum-aware training-free resolution promotion method that dynamically adapts positional scaling across denoising steps via a rational decay scheduler and a time-dependent frequency ramp. Its resolution-agnostic formulation enables robust multi-scale extrapolation from a single set of hyperparameters, consistently outperforming all training-free baselines

across six resolutions with negligible computational overhead.

II. RELATED WORK

A. Remote Sensing Image Generation

Generative modeling for RS imagery has evolved from GAN-based methods [18] to diffusion-based frameworks [15, 19]. Early work targeted task-specific problems such as super-resolution [2], cloud removal [4], image translation [3], and scene-conditioned synthesis [5, 20], demonstrating the value of generative priors but not addressing open-ended text-to-image generation.

In the natural-image domain, Latent Diffusion Models [21] introduced efficient diffusion in a compressed latent space, later scaled by SDXL [22] with multi-resolution training and refined architectures. Controllable conditioning mechanisms such as ControlNet [23] further enriched spatial control over generated content. Recent diffusion-based RS methods [7, 19] improved generation fidelity, yet most adopt U-Net backbones optimized for patch-level generation or conditional restoration, ill-suited for large-scale synthesis requiring both global spatial organization and fine-grained semantic modeling. The success of DiTs [1] suggests a promising direction, but the RS community still lacks a DiT checkpoint for text-to-image generation, motivating our RS-specific FLUX [17] model.

B. Training-Free Resolution Promotion

Rotary Position Embedding (RoPE) [11] preserves relative positional structure while remaining compatible with scalable self-attention, making it the standard positional encoding in recent DiTs [1, 17]. When a model trained at a limited resolution is applied to a much larger image, positional indices exceed the training range, introducing a positional out-of-distribution (OOD) effect that destabilizes attention patterns [12, 14].

Training-free methods address this OOD problem by rescaling RoPE frequencies at inference time. Position Interpolation (PI) [12] compresses all frequencies uniformly; NTK-aware scaling [13] adjusts the base wavelength; YaRN [14] applies a frequency-selective ramp that distinguishes low- from high-frequency modes. These methods are computationally attractive and provide a practical starting point for large-scale generation. However, they are primarily developed and validated on natural images and large language models [12, 14], without accounting for the unique spectral characteristics of RS imagery.

Beyond RoPE rescaling, alternative training-free approaches target higher-resolution generation from different angles. ScaleCrafter [24] re-dilates convolutional kernels to enlarge the effective receptive field without retraining, while DemoFusion [25] employs progressive upscaling with skip connections from coarser resolutions. Although effective for U-Net-based architectures, these methods operate on convolution-centric designs and do not address the positional out-of-distribution problem that arises in RoPE-based DiTs, making them orthogonal rather than directly comparable to our approach.

C. Limitations of Static Extrapolation for RS Synthesis

All aforementioned methods apply a static scaling rule throughout the denoising process [12–14], ignoring its temporal dynamics. Early high-noise steps establish coarse layout, whereas late low-noise steps recover high-frequency details [15, 16]. RS images contain denser high-frequency structures than natural images [9, 26]; a time-invariant rule uniformly compresses the positional spectrum, preserving large-scale layout but under-representing the high-frequency information critical for RS realism.

Our work differs in two respects: we provide a domain-specialized DiT prior for RS, and we introduce a spectrum-aware dynamic adaptation strategy that varies with denoising time, aligning extrapolation strength with the frequency-progressive generation process.

III. METHODOLOGY

Our framework addresses large-scale RS text-to-image synthesis in two steps. We first fine-tune FLUX [17] on curated RS data to obtain a domain-specialized prior, **RS-FLUX** (Sec. III-A). At inference time, we then apply **SHARP**, which dynamically modifies the Rotary Position Embedding (RoPE) [11] frequencies within RS-FLUX to enable training-free resolution promotion, as illustrated in Fig. 4. The design of SHARP is grounded in two observations: RS imagery carries substantially denser high-frequency energy than natural images, and diffusion denoising recovers different frequency bands at different stages, with low-frequency layout emerging early and high-frequency details crystallizing late. These observations motivate a strong-to-weak scheduling rule for positional scaling.

A. RS-Specialized Foundation Model

Open-source DiT checkpoints [1] are optimized for natural images and do not adequately capture the semantics and spectral statistics of aerial scenes. RS imagery contains dense man-made structures, small objects, and repetitive textures that are under-represented by natural-image priors [26]. While parameter-efficient approaches such as LoRA [27] offer lightweight domain adaptation, we opt for full fine-tuning of FLUX [17] on a curated dataset of over 100,000 high-quality RS images to maximize the model’s capacity to capture the distinctive spectral and geometric properties of RS imagery. The resulting model, **RS-FLUX**, serves as the base generator in all experiments. Since SHARP is applied only at inference time, no additional high-resolution retraining is required.

B. Spectral Motivation and Frequency-Progressive Denoising

To motivate the dynamic promotion strategy, we first quantify the spectral discrepancy between natural and RS images. Following the protocol detailed in Fig. 2, we compute the average normalized radial PSD over 100 ImageNet [26] and 100 DIOR [9] images. After low-frequency normalization, RS imagery retains substantially stronger energy in medium- and high-frequency bands (Fig. 2), corresponding to vehicles, roof boundaries, and dense urban textures. This discrepancy implies

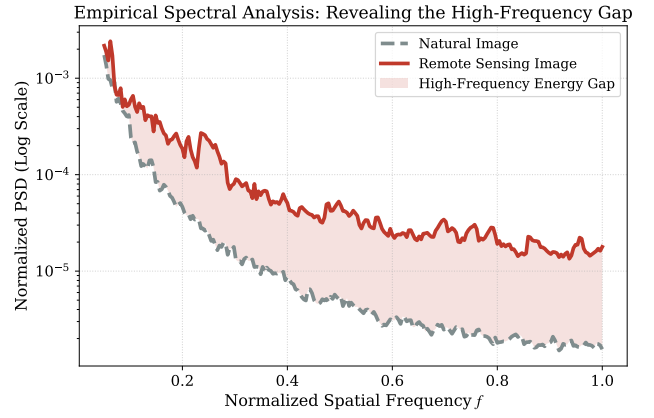


Fig. 2. **Empirical Spatial Spectrum Analysis.** Average normalized radial power spectral density (PSD) over 100 ImageNet [26] images and 100 DIOR [9] images. Each image is converted to grayscale, resized to 512×512 , windowed by a 2-D Hanning function, transformed by a centered FFT, radially averaged, and normalized by its non-DC low-frequency baseline. RS imagery exhibits systematically stronger medium- and high-frequency energy than natural imagery.

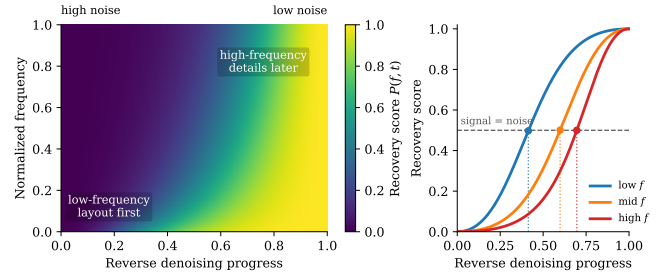


Fig. 3. **Frequency-Progressive Denoising.** Left: heatmap of the bounded recovery score $P(f, t) = \rho(f, t)/(1 + \rho(f, t))$ over normalized frequency and reverse denoising progress. Lower-frequency bands enter the signal-dominant regime earlier than higher-frequency bands. Right: representative trajectories for low-, medium-, and high-frequency components, whose threshold crossings occur progressively later. This progression motivates strong early promotion and weaker late extrapolation.

that a strategy uniformly compressing the spatial spectrum is more damaging for RS than for natural-image generation.

This empirical analysis establishes *what* differs between the two domains; we next analyze *when* different frequency bands become recoverable during generation. Following the flow-matching formulation [28] used by FLUX [17], the noisy latent at normalized time $t \in [0, 1]$ is

$$x_t = (1 - t)x_0 + t\epsilon, \quad (1)$$

where $x_0 \sim p_{\text{data}}$ and $\epsilon \sim \mathcal{N}(0, I)$. Applying the Fourier transform yields

$$\hat{x}_t = (1 - t)\hat{x}_0 + t\hat{\epsilon}. \quad (2)$$

Assuming independence between \hat{x}_0 and $\hat{\epsilon}$ with white noise spectrum, the expected PSD at spatial frequency f is

$$\mathbb{E}[\|\hat{x}_t\|_f^2] = (1 - t)^2 S(f) + t^2 C_\epsilon, \quad (3)$$

where $S(f) = \mathbb{E}[\|\hat{x}_0\|_f^2]$ is the clean data PSD and C_ϵ is a frequency-independent noise constant.

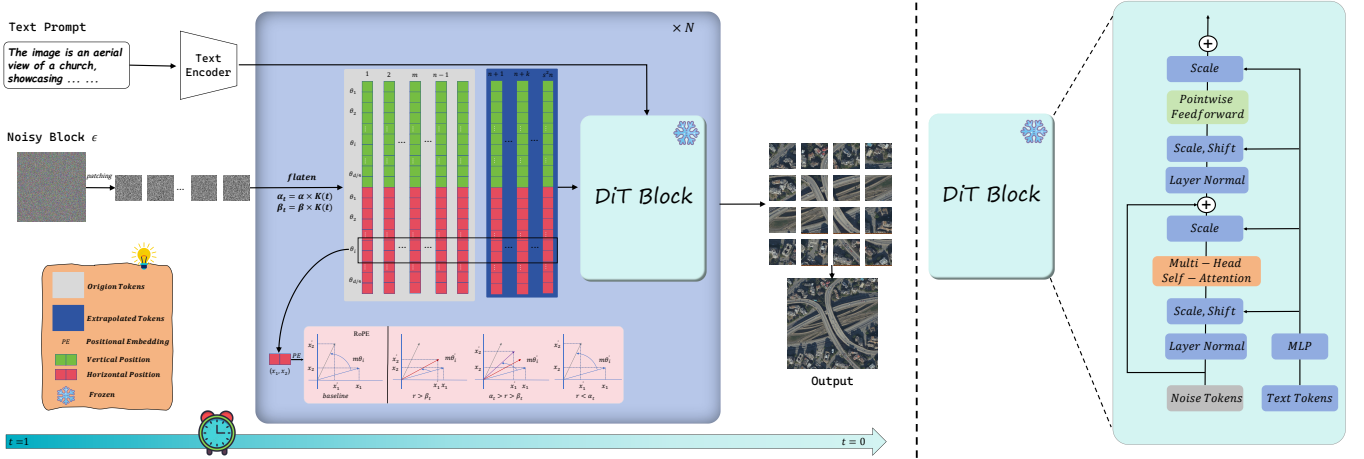


Fig. 4. **SHARP Overview.** SHARP performs dynamic resolution promotion in RoPE through the time-dependent scheduler $\kappa_{RS}(t)$ and the ramp function $\gamma(r, t)$. Strong promotion is preserved in the early layout stage and progressively reduced in the late detail-recovery stage, avoiding the over-smoothing caused by static extrapolation.

Each frequency band is governed by a competition between the clean signal and the noise floor. We define the signal-dominance ratio

$$\rho(f, t) = \frac{(1-t)^2 S(f)}{t^2 C_\epsilon}. \quad (4)$$

Since $S(f)$ decreases with frequency, for any $f_l < f_h$ we have $\rho(f_l, t) > \rho(f_h, t)$, meaning lower-frequency bands become signal-dominant earlier. For visualization, we define the bounded recovery score

$$P(f, t) = \frac{\rho(f, t)}{1 + \rho(f, t)} \in [0, 1], \quad (5)$$

where larger values indicate greater signal dominance. Fig. 3 visualizes this quantity over normalized frequency and reverse denoising progress.

The critical transition time $t_c(f)$, at which signal and noise are equally strong ($\rho(f, t_c) = 1$), is

$$t_c(f) = \frac{\sqrt{S(f)}}{\sqrt{S(f)} + \sqrt{C_\epsilon}}. \quad (6)$$

Because $t_c(f)$ increases with $S(f)$ and $S(f)$ decreases with frequency, low-frequency components emerge earlier while high-frequency details become recoverable mainly in the terminal stage. Combined with the empirical finding that RS imagery has inherently stronger high-frequency energy (Fig. 2), this frequency-progressive behavior provides a two-fold motivation for dynamic resolution promotion: RS images are both more reliant on high-frequency fidelity and more vulnerable to its suppression by static extrapolation.

C. SHARP: Dynamic Resolution Promotion

The above analysis reveals a fundamental limitation of static RoPE extrapolation [12–14]: a time-invariant scaling rule helps in the early stage where large receptive fields organize global layout, but becomes harmful in the late stage where the same spectral compression suppresses the high-frequency

components most important for RS detail recovery. Large-scale RS generation therefore requires a dynamic extrapolation strategy.

SHARP addresses this limitation through a spectrum-aware dynamic resolution promotion mechanism in the RoPE space. As illustrated in the inference pipeline of Fig. 4, at each denoising step SHARP modifies the RoPE frequency table through two coupled modules: (i) the *Rational Decay Scheduler* (RDS), which governs how promotion strength evolves over denoising time, and (ii) the *Dynamic Ramp Function*, which allocates differential treatment to different frequency modes based on the current scheduler state.

Rational Decay Scheduler (RDS). The RDS maps the normalized timestep to a decaying coefficient:

$$\kappa_{RS}(t) = \frac{t}{\alpha_s - (\alpha_s - 1)t}, \quad \alpha_s \geq 1, \quad (7)$$

which smoothly decays from near-unity to zero. As visualized by the scheduler curve in Fig. 4, when t is large (early denoising), $\kappa_{RS}(t) \approx 1$, preserving strong promotion for layout formation; as $t \rightarrow 0$ (late denoising), $\kappa_{RS}(t) \rightarrow 0$, releasing the model from excessive positional compression in the terminal stage.

Dynamic ramp function. Using $\kappa_{RS}(t)$, we define the time-dependent transition boundaries that control the frequency-domain partitioning shown in Fig. 4:

$$\alpha_t = \alpha \cdot \kappa_{RS}(t), \quad \beta_t = \beta \cdot \kappa_{RS}(t), \quad (8)$$

which control the effective promotion range at denoising time t .

Let $s = L_{\text{target}}/L_{\text{train}}$ denote the resolution promotion factor. For the d -th RoPE component with base frequency θ_d and corresponding wavelength λ_d , define the normalized frequency ratio

$$r(d) = \frac{L_{\text{target}}}{\lambda_d}. \quad (9)$$

SHARP rescales each RoPE frequency through the time-dependent interpolation

$$h_t(\theta_d) = (1 - \gamma(r(d), t)) \frac{\theta_d}{s} + \gamma(r(d), t) \theta_d, \quad (10)$$

where $\gamma(r, t)$ is a dynamic ramp function:

$$\gamma(r, t) = \begin{cases} 0, & r < \alpha_t, \\ \frac{r - \alpha_t}{\beta_t - \alpha_t}, & \alpha_t \leq r \leq \beta_t, \\ 1, & r > \beta_t. \end{cases} \quad (11)$$

Equation 10 shows that low- r modes receive the extrapolated frequency θ_d/s , high- r modes retain θ_d , and the intermediate band is smoothly interpolated. SHARP thus allocates strong promotion to structure-oriented modes and progressively restores uncompressed higher-frequency modes as denoising proceeds.

This design directly reflects the frequency-progressive behavior derived in Sec. III-B. As depicted in the temporal progression of Fig. 4, in the early stage ($t \approx 1$), $\kappa_{rs}(t) \approx 1$ keeps the transition band wide, applying strong promotion for layout formation. In the late stage ($t \rightarrow 0$), $\kappa_{rs}(t)$ decreases toward zero, narrowing the promoted band and shifting more frequency modes toward the uncompressed regime, thereby preserving the native high-frequency content required for RS detail recovery. Within a unified RoPE formulation, SHARP thus performs strong structural extrapolation early and high-frequency preservation late.

Algorithm 1 summarizes the complete SHARP inference procedure.

Multi-scale compatibility. A notable property of SHARP is its inherent resolution-agnostic design. Because $\kappa_{rs}(t)$ is defined on the normalized timestep $t \in [0, 1]$ and the ramp function $\gamma(r, t)$ operates on the dimensionless frequency ratio $r(d) = L_{\text{target}}/\lambda_d$, the entire formulation is independent of absolute pixel dimensions. When the target resolution changes, only the promotion factor $s = L_{\text{target}}/L_{\text{train}}$ is updated; the scheduler and ramp hyperparameters (α_s, α, β) remain fixed. This enables a single parameter configuration to serve diverse square and rectangular extrapolation factors without per-resolution tuning, as empirically verified across six resolutions in Sec. IV.

IV. EXPERIMENTS

A. Experimental Setup

1) *Training Data Construction:* We construct a domain-specialized corpus from the GeoChat dataset [29], which provides RS images with multi-turn dialogues. Since the question-answer format is poorly aligned with caption-style supervision, we use Qwen-VL [30] to convert each sample into a compact prompt-image pair (Fig. 7, right). This yields 102,952 pairs for RS-FLUX fine-tuning. The dataset spans multiple resolutions (Fig. 7, left), helping the model learn a prior robust to different spatial extents.

Algorithm 1 SHARP Inference

Require: Trained RS-FLUX model \mathcal{F} ; text prompt c ; target size L_{target} ; training size L_{train} ; scheduler coefficient α_s ; transition bounds α, β ; denoising timesteps $\{t_n\}_{n=0}^N$ with $t_0 = 1, t_N = 0$

Ensure: Generated image \hat{x}_0 at resolution L_{target}

```

1:  $s \leftarrow L_{\text{target}}/L_{\text{train}}$   $\triangleright$  Resolution promotion factor
2:  $x_{t_0} \sim \mathcal{N}(0, I)$   $\triangleright$  Initialize noise at target resolution
3: for  $n = 0$  to  $N - 1$  do
4:    $\kappa_{rs}(t_n) \leftarrow t_n / [\alpha_s - (\alpha_s - 1) t_n]$   $\triangleright$  Rational Decay Scheduler
5:    $\alpha_{t_n} \leftarrow \alpha \cdot \kappa_{rs}(t_n)$ ;  $\beta_{t_n} \leftarrow \beta \cdot \kappa_{rs}(t_n)$   $\triangleright$  Dynamic bounds
6:   for each RoPE dimension  $d$  do
7:      $r(d) \leftarrow L_{\text{target}}/\lambda_d$ 
8:      $\gamma \leftarrow \text{clamp}((r(d) - \alpha_{t_n}) / (\beta_{t_n} - \alpha_{t_n}), 0, 1)$   $\triangleright$  Dynamic ramp
9:      $h_{t_n}(\theta_d) \leftarrow (1 - \gamma) \theta_d/s + \gamma \theta_d$   $\triangleright$  Rescaled frequency
10:  end for
11:  Apply  $\{h_{t_n}(\theta_d)\}_d$  to RoPE in  $\mathcal{F}$ 
12:   $x_{t_{n+1}} \leftarrow \text{Denoise}(\mathcal{F}, x_{t_n}, t_n, c)$   $\triangleright$  One denoising step
13: end for
14:  $\hat{x}_0 \leftarrow \text{Decode}(x_{t_N})$   $\triangleright$  VAE decode
15: return  $\hat{x}_0$ 

```

2) *Evaluation Protocol:* We build a benchmark of 100 prompts generated by GPT-5.4 [31], covering representative RS scenes and diverse spatial compositions. All methods are evaluated on the same prompt set with the same RS-FLUX checkpoint and sampling configuration, isolating the effect of the resolution promotion strategy.

We adopt three reference-free metrics: CLIP Score [32] for text-image semantic consistency, Aesthetic Score (Aes) [33] for perceptual quality, and HPSv2 [34] for human preference alignment. Higher values indicate better performance for all three metrics.

3) *Multi-Scale Extrapolation Setting:* Since RS-FLUX is trained at 1024×1024 , we evaluate on larger targets: square resolutions of 1536^2 ($1.5\times$), 2048^2 ($2\times$), 2560^2 ($2.5\times$), and rectangular resolutions of 2048×1536 , 2560×1920 , 3072×2048 . All methods generate images from the same 100 prompts under identical seeds.

4) *Implementation Details:* RS-FLUX is fine-tuned from the public FLUX checkpoint at the native training resolution of 1024×1024 . We use AdamW ($\beta_1=0.9$, $\beta_2=0.999$, weight decay 0.01) with a learning rate of 1×10^{-5} and cosine annealing. The effective batch size is 64 via gradient accumulation across 8 NVIDIA A6000 48 GB GPUs with bf16 mixed precision. Training runs for 10K steps. During inference, all compared methods share the same text encoder, diffusion backbone, VAE, prompt set, random seeds, Euler sampler with 50 denoising steps, and a guidance scale of 3.5. The only difference lies in the positional extrapolation strategy, ensuring that performance gaps are attributable solely to RoPE adaptation. For SHARP, the default hyperparameters

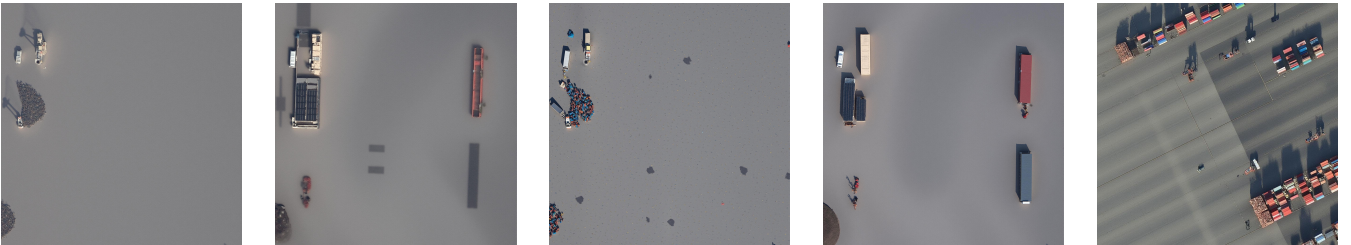
A high-resolution aerial view of a complex multi-level concrete highway overpass. Countless vehicles are actively driving along the interlocking asphalt lanes and curved ramps. The background is completely filled with densely built urban architecture, paved concrete roads, and grey rooftops.



Top-down aerial view of a petrochemical industrial facility. Numerous large, white cylindrical oil storage tanks are arranged symmetrically on a barren, paved industrial lot. The concrete area is intersected by a complex network of metal pipelines and service roads.



Top-down satellite view of a busy logistic shipping yard. Heavy transport trucks and container handlers are operating on a vast expanse of industrial asphalt. The scene is dominated by geometric stacks of cargo and grey concrete surfaces.



RS-Flux

PI

NTK-aware

YaRN

SHARP_(ours)

Fig. 5. **Qualitative comparison at 2048×2048 .** From left to right: RS-FLUX (baseline), PI, NTK-aware, YaRN, and SHARP. Red boxes indicate zoom-in regions shown in each inset. SHARP produces more complete large-scale layouts and preserves sharper RS-specific details, including road topology, storage-tank boundaries, vehicles, and cargo structures.

TABLE I
NATIVE-RESOLUTION COMPARISON AT 1024×1024 . HIGHER IS BETTER.

Model	CLIP \uparrow	Aes \uparrow	HPSv2 \uparrow
FLUX (vanilla)	25.53	5.18	0.236
RS-FLUX (ours)	28.62	5.97	0.283

are $\alpha_s=3$, $\alpha=1$, and $\beta=32$, as determined by the ablation study in Sec. IV-E.

B. RS-FLUX Validation at Native Resolution

Before evaluating resolution promotion strategies, we verify that RS-specific fine-tuning improves generation quality at the native 1024×1024 resolution. Table I compares vanilla FLUX with RS-FLUX on the same 100-prompt benchmark without positional extrapolation.

RS-FLUX outperforms vanilla FLUX by +3.09 CLIP Score, +0.79 Aes, and +0.047 HPSv2, confirming that domain-specific fine-tuning substantially improves RS generation quality and provides a stronger starting point for large-scale extrapolation.

C. Quantitative Comparison

Table II compares SHARP with four training-free baselines across all six resolutions and three metrics.

Overall performance. SHARP reaches 27.54 CLIP, 5.78 Aes, and 0.270 HPSv2 on average, outperforming the strongest baseline YaRN by +0.39/+0.13/+0.008 and RS-FLUX by +1.47/+0.44/+0.029.

Square extrapolation. SHARP improves over YaRN from 27.27/5.68/0.263 to 27.68/5.81/0.271. The margin widens with extrapolation factor: +0.32/+0.11/+0.007 at 1536^2 to +0.50/+0.14/+0.009 at 2560^2 , indicating increasing benefit as the positional OOD effect becomes more severe. From 1536^2 to 2560^2 , SHARP's metrics degrade by only 0.75/0.18/0.010 versus 0.93/0.21/0.012 for YaRN.

Rectangular extrapolation. SHARP remains best at all rectangular settings, with gains over YaRN of +0.33 to +0.43 CLIP and the largest margins at the most challenging 3072×2048 (26.93/5.64/0.263 vs. 26.50/5.50/0.254). Notably, the anisotropic setting introduces additional difficulty because the extrapolation factor differs along the two spatial axes, yet SHARP handles this gracefully since its RoPE rescaling operates independently on each axis through the same dimen-

A satellite image of a rural market town with dense shop blocks, a bus station, surrounding crop fields, narrow feeder roads, and mixed residential and commercial parcels-



Satellite imagery showing a modern downtown beside a wide river, several bridges linking both banks, office towers casting long shadows, riverside parks, and dense commercial blocks arranged along the waterfront-



Fig. 6. **Multi-scale generation from a single prompt.** Each row uses the same text prompt to generate RS images across six resolutions covering both square and rectangular aspect ratios: 1024×1024 (native), 1536×1536 , 2048×2048 , 2560×2560 , 1706×2560 , and 3756×2560 . Despite the substantial variation in spatial extent and aspect ratio, SHARP preserves global semantic consistency: scene-level composition, object spatial relationships, and dominant structural layouts remain stable across all scales. Simultaneously, higher resolutions progressively reveal finer RS-specific details, including individual vehicle silhouettes, building footprint edges, and road surface textures, that are unresolvable at smaller scales. This consistent structural coherence combined with faithful detail enrichment validates that SHARP’s dynamic RoPE scheduling successfully decouples layout organization from high-frequency recovery, enabling robust multi-scale extrapolation from a single trained resolution.

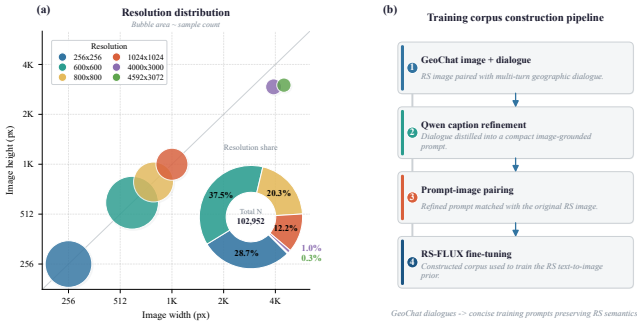


Fig. 7. **Overview of the RS text-to-image training corpus.** Left: bubble-chart visualization of the 102,952-sample resolution distribution. Bubble position indicates width and height; area reflects sample count. The inset donut chart summarizes the composition by resolution and displays the total corpus size. Right: construction pipeline. For each GeoChat sample, the RS image and its dialogue are fed to Qwen-VL to synthesize a compact caption, yielding prompt-image pairs for RS-FLUX fine-tuning.

sionless frequency ratio $r(d)$.

D. Qualitative Comparison

Fig. 5 presents representative results at 2048×2048 . Static baselines produce over-smoothed outputs: in the *highway overpass* scene, they yield blurred lane boundaries and simplified ramp topology; in the *petrochemical facility*, weak storage-tank contours and schematic layouts; in the *logistics yard*, flat asphalt-like regions with sparse object traces. YaRN improves scene organization but remains relatively smooth in detail-critical regions. SHARP further preserves multi-level road continuity, clearer tank boundaries, and sharper vehicles

and cargo stacks, confirming that dynamic RoPE adaptation outperforms static extrapolation by maintaining strong layout promotion early while avoiding excessive suppression of high-frequency details late.

Fig. 6 demonstrates SHARP’s multi-scale consistency. Using the same prompt, SHARP generates RS images across six resolutions from the native 1024×1024 to 3756×2560 , spanning both square and rectangular aspect ratios. Across all scales, SHARP maintains coherent spatial composition while progressively revealing finer details, including vehicle contours, building boundaries, and road textures, as resolution increases. Crucially, the spatial relationships between objects remain stable even as the canvas expands substantially and the aspect ratio changes, indicating that the dynamic scheduler successfully anchors global layout before releasing high-frequency modes. This validates that the RDS ensures consistent layout organization while the dynamic ramp preserves scale-appropriate high-frequency content.

E. Ablation Studies

We conduct ablation experiments at 2048×2048 to validate each design choice. All ablations use the same 100-prompt benchmark.

Table III(a) confirms that RS-specific fine-tuning and SHARP are complementary: each independently improves over vanilla FLUX, and their combination yields the best results (+2.89 CLIP over vanilla). Notably, SHARP alone on vanilla FLUX (26.15 CLIP) already approaches the performance of RS-FLUX without SHARP (26.21 CLIP), demonstrating that dynamic positional adaptation provides substantial

TABLE II

MULTI-SCALE QUANTITATIVE COMPARISON UNDER SQUARE AND RECTANGULAR EXTRAPOLATION. HIGHER IS BETTER FOR ALL METRICS. THE UPPER BLOCK EVALUATES SQUARE EXTRAPOLATION; THE LOWER BLOCK EVALUATES RECTANGULAR EXTRAPOLATION. "OVERALL AVG." AVERAGES ALL SIX RESOLUTIONS.

Square Extrapolation												
Method	1536 × 1536			2048 × 2048			2560 × 2560			Square Avg.		
	CLIP↑	Aes↑	HPSv2↑									
RS-FLUX (baseline)	26.84	5.48	0.249	26.21	5.36	0.242	25.57	5.25	0.236	26.21	5.36	0.242
PI	27.18	5.56	0.255	26.73	5.46	0.248	26.09	5.33	0.241	26.67	5.45	0.248
NTK-aware	27.44	5.63	0.261	27.02	5.54	0.255	26.46	5.42	0.248	26.97	5.53	0.255
YaRN	27.71	5.78	0.269	27.31	5.69	0.263	26.78	5.57	0.257	27.27	5.68	0.263
SHARP (ours)	28.03	5.89	0.276	27.72	5.82	0.271	27.28	5.71	0.266	27.68	5.81	0.271
Rectangular Extrapolation												
Method	2048 × 1536			2560 × 1920			3072 × 2048			Overall Avg.		
	CLIP↑	Aes↑	HPSv2↑									
RS-FLUX (baseline)	26.48	5.42	0.246	25.94	5.31	0.239	25.38	5.20	0.233	26.07	5.34	0.241
PI	26.96	5.50	0.252	26.42	5.40	0.246	25.88	5.28	0.239	26.54	5.42	0.247
NTK-aware	27.25	5.58	0.259	26.74	5.48	0.252	26.19	5.36	0.245	26.85	5.50	0.253
YaRN	27.53	5.72	0.267	27.04	5.62	0.261	26.50	5.50	0.254	27.15	5.65	0.262
SHARP (ours)	27.86	5.84	0.274	27.40	5.75	0.269	26.93	5.64	0.263	27.54	5.78	0.270

TABLE III

ABLATION STUDIES AT 2048 × 2048. HIGHER IS BETTER. CL = CLIP SCORE, AE = AESTHETIC SCORE, HP = HPSV2. (A) COMPONENT CONTRIBUTIONS (FT = FINE-TUNING, SH = SHARP). (B) SCHEDULER FORM. (C) SCHEDULER COEFFICIENT α_s . (D) TRANSITION BOUNDS (α, β) .

(a) Component					(b) Scheduler form				(c) Coefficient α_s				(d) Bounds (α, β)				
FT	SH	CL	Ae	HP	Schedule	CL	Ae	HP	α_s	CL	Ae	HP	α	β	CL	Ae	HP
		24.83	5.08	.228	Static	27.35	5.70	.264	1	27.48	5.74	.266	1	16	27.45	5.71	.264
	✓	26.15	5.48	.253	Linear	27.48	5.74	.266	2	27.61	5.78	.269	1	32	27.72	5.82	.271
	✓	26.21	5.36	.242	Cosine	27.58	5.77	.268	3	27.72	5.82	.271	2	32	27.61	5.77	.268
✓	✓	27.72	5.82	.271	Rational	27.72	5.82	.271	4	27.55	5.75	.267	2	64	27.38	5.66	.261

gains even without domain-specific training. This complementarity arises because fine-tuning enriches the domain-specific semantic prior while SHARP addresses the orthogonal positional OOD problem at inference time; the two mechanisms operate on different aspects of the generation pipeline and thus compound rather than overlap.

Panel (b) compares four scheduling strategies for $\kappa(t)$, all satisfying $\kappa(1)=1$ and $\kappa(0)=0$ with identical transition bounds $(\alpha, \beta)=(1, 32)$. Even the simplest dynamic schedule (linear) outperforms the static baseline by +0.13 CLIP, confirming that time-varying extrapolation is universally beneficial. The rational form achieves the best performance by maintaining near-unity promotion through the mid-stage before decaying rapidly near $t=0$, best matching the frequency-progressive nature of diffusion denoising. The cosine schedule shares a similar decay profile but transitions less sharply in the terminal phase, resulting in slightly weaker high-frequency preservation.

Panel (c) reveals a unimodal optimum at $\alpha_s=3$, controlling how aggressively the rational scheduler decays. At $\alpha_s=1$ (equivalent to linear decay), promotion decreases too gradually, causing residual positional compression in the late stage;

at $\alpha_s=4$, promotion is released too early, weakening mid-stage layout formation. The $\alpha_s=1$ result (27.48/5.74/.266) exactly matches the linear entry in panel (b), as the two formulations are mathematically equivalent, providing independent cross-validation.

Panel (d) confirms $(\alpha, \beta)=(1, 32)$ as optimal, coinciding with YaRN’s default ramp parameters [14] originally selected for LLM context extension. This suggests that the frequency-domain partition is robust across modalities and that SHARP’s gains stem from the orthogonal temporal scheduling dimension rather than from re-tuning the ramp boundaries. When β is too small ($\beta=16$), the transition band is narrow and most modes bypass promotion; when β is too large ($\beta=64$), nearly all modes are uniformly interpolated, losing the frequency-selective advantage.

F. Computational Efficiency

SHARP modifies only the RoPE frequency computation at each step, introducing no additional parameters or layers. Table IV reports inference time on a single A6000 GPU.

SHARP adds less than 1.5% wall-clock overhead (<1.0% at 2560²), since the RoPE rescaling involves only element-wise

TABLE IV
INFERENCE COST (SECONDS PER IMAGE). PEAK GPU MEMORY IS
IDENTICAL ACROSS ALL METHODS.

Method	1536 ²	2048 ²	2560 ²
RS-FLUX	51.5	98.0	176.7
PI	52.1	98.1	177.1
NTK-aware	52.7	98.4	177.9
YaRN	52.9	99.2	178.2
SHARP	53.1	99.4	178.4

arithmetic negligible relative to the full transformer forward pass.

Limitations. Our evaluation relies on reference-free metrics; broader human studies or downstream RS task validation (e.g., object detection on synthesized data) would strengthen the evidence. Additionally, while the rational scheduler proves effective, exploring adaptive or learned schedules conditioned on input prompts may further improve robustness. Finally, very large target resolutions still incur substantial inference cost due to the quadratic attention complexity inherent to all transformer-based methods.

V. CONCLUSION

We present SHARP, a spectrum-aware training-free resolution promotion framework for large-scale RS text-to-image synthesis. Our approach addresses two coupled challenges: the lack of a domain-specialized DiT prior and the failure of static positional extrapolation to preserve the dense high-frequency content characteristic of RS imagery. By fine-tuning FLUX on 102,952 curated RS prompt-image pairs and introducing a dynamic RoPE extrapolation strategy governed by a rational decay scheduler $\kappa_{r,s}(t)$, SHARP aligns positional scaling with the frequency-progressive nature of diffusion denoising.

Extensive experiments across six square and rectangular resolutions demonstrate that SHARP consistently outperforms all training-free baselines in CLIP Score, Aesthetic Score, and HPSv2, with widening margins at more aggressive extrapolation factors and negligible computational overhead (<1.5%). The resolution-agnostic formulation enables robust multi-scale generation from a single set of hyperparameters, and comprehensive ablation studies confirm that domain-specific fine-tuning and dynamic scheduling are complementary, with each design choice validated independently. Future directions include expanding the RS corpus, exploring prompt-conditioned dynamic schedules, and integrating efficient attention mechanisms to reduce inference cost at very large resolutions.

REFERENCES

- [1] W. Peebles and S. Xie, "Scalable diffusion models with transformers," in *Proceedings of the IEEE/CVF international conference on computer vision*, 2023, pp. 4195–4205.
- [2] C. Saharia, J. Ho, W. Chan, T. Salimans, D. J. Fleet, and M. Norouzi, "Image super-resolution via iterative refinement," 2021. [Online]. Available: <https://arxiv.org/abs/2104.07636>
- [3] B. Zhao, C. Yang, Q. Zhou, and Q. Wang, "Rli-dm: Robust layout-based iterative diffusion model for sar-to-rgb image translation," *IEEE Transactions on Geoscience and Remote Sensing*, 2025.
- [4] J. Sui, Y. Ma, W. Yang, X. Zhang, M.-O. Pun, and J. Liu, "Diffusion enhancement for cloud removal in ultra-resolution remote sensing imagery," 2024. [Online]. Available: <https://arxiv.org/abs/2401.15105>
- [5] C. Yang, B. Zhao, Q. Zhou, and Q. Wang, "Mmo-ig: Multi-class and multi-scale object image generation for remote sensing," *IEEE Transactions on Geoscience and Remote Sensing*, 2025.
- [6] D. Tang, X. Cao, X. Hou, Z. Jiang, J. Liu, and D. Meng, "Crs-diff: Controllable remote sensing image generation with diffusion model," 2024. [Online]. Available: <https://arxiv.org/abs/2403.11614>
- [7] A. Sebaq and M. ElHelw, "Rsdiff: Remote sensing image generation from text using diffusion model," *Neural Computing and Applications*, vol. 36, no. 36, pp. 23 103–23 111, 2024.
- [8] M. Göktepe, A. Shamseddin, E. Uysal, J. Monteagudo, L. Drees, A. Toker, S. Asseng, and M. von Bloh, "Ecomapper: Generative modeling for climate-aware satellite imagery," in *Proceedings of the 42nd International Conference on Machine Learning (ICML)*, July 2025.
- [9] K. Li, G. Wan, G. Cheng, L. Meng, and J. Han, "Object detection in optical remote sensing images: A survey and a new benchmark," *ISPRS journal of photogrammetry and remote sensing*, vol. 159, pp. 296–307, 2020.
- [10] R. Ou, Y. Hu, F. Zhang, J. Chen, and Y. Liu, "Geopix: Multi-modal large language model for pixel-level image understanding in remote sensing," 2025. [Online]. Available: <https://arxiv.org/abs/2501.06828>
- [11] J. Su, M. Ahmed, Y. Lu, S. Pan, W. Bo, and Y. Liu, "Roformer: Enhanced transformer with rotary position embedding," *Neurocomputing*, vol. 568, p. 127063, 2024.
- [12] S. Chen, S. Wong, L. Chen, and Y. Tian, "Extending context window of large language models via positional interpolation," *arXiv preprint arXiv:2306.15595*, 2023.
- [13] bloc97, "Ntk-aware scaled rope allows llama models to have extended (8k+) context size without any fine-tuning and minimal perplexity degradation," <https://www.reddit.com/r/LocalLLaMA/comments/14lz7j5/>, 2023.
- [14] B. Peng, J. Quesnelle, H. Fan, and E. Shippole, "Yarn: Efficient context window extension of large language models," *arXiv preprint arXiv:2309.00071*, 2023.
- [15] J. Ho, A. Jain, and P. Abbeel, "Denoising diffusion probabilistic models," *Advances in neural information processing systems*, vol. 33, pp. 6840–6851, 2020.
- [16] Y. Song, J. Sohl-Dickstein, D. P. Kingma, A. Kumar, S. Ermon, and B. Poole, "Score-based generative modeling through stochastic differential equations," *arXiv preprint arXiv:2011.13456*, 2020.
- [17] Black Forest Labs, "Flux.1: A 12 billion parameter rectified flow transformer for text-to-image generation," <https://github.com/black-forest-labs/flux>, 2024.
- [18] J. Li, K. Chen, L. Liu, Z. Zou, and Z. Shi, "Dual-

- branch gan for cloud image generation based on cloud and background decoupling,” *Chinese Space Science and Technology*, vol. 45, no. 5, pp. 49–59, 2025.
- [19] Z. Yu, C. Liu, L. Liu, Z. Shi, and Z. Zou, “Metaearth: A generative foundation model for global-scale remote sensing image generation,” 2024. [Online]. Available: <https://arxiv.org/abs/2405.13570>
- [20] D. Tang, X. Cao, X. Wu, J. Li, J. Yao, X. Bai, D. Jiang, Y. Li, and D. Meng, “Aerogen: Enhancing remote sensing object detection with diffusion-driven data generation,” 2025. [Online]. Available: <https://arxiv.org/abs/2411.15497>
- [21] R. Rombach, A. Blattmann, D. Lorenz, P. Esser, and B. Ommer, “High-resolution image synthesis with latent diffusion models,” in *Proceedings of the IEEE/CVF conference on computer vision and pattern recognition*, 2022, pp. 10 684–10 695.
- [22] D. Podell, Z. English, K. Lacey, A. Blattmann, T. Dockhorn, J. Müller, J. Penna, and R. Rombach, “Sdxl: Improving latent diffusion models for high-resolution image synthesis,” *arXiv preprint arXiv:2307.01952*, 2023.
- [23] L. Zhang, A. Rao, and M. Agrawala, “Adding conditional control to text-to-image diffusion models,” in *Proceedings of the IEEE/CVF international conference on computer vision*, 2023, pp. 3836–3847.
- [24] Y. He, S. Yang, H. Chen, X. Cun, M. Xia, Y. Zhang, X. Wang, R. He, Q. Chen, and Y. Shan, “Scalecrafter: Tuning-free higher-resolution visual generation with diffusion models,” in *The Twelfth International Conference on Learning Representations*, 2023.
- [25] R. Du, D. Chang, T. Hospedales, Y.-Z. Song, and Z. Ma, “Demofusion: Democratising high-resolution image generation with no \$\$\$,” in *Proceedings of the IEEE/CVF conference on computer vision and pattern recognition*, 2024, pp. 6159–6168.
- [26] J. Deng, W. Dong, R. Socher, L.-J. Li, K. Li, and L. Fei-Fei, “Imagenet: A large-scale hierarchical image database,” in *2009 IEEE conference on computer vision and pattern recognition*. Ieee, 2009, pp. 248–255.
- [27] E. J. Hu, Y. Shen, P. Wallis, Z. Allen-Zhu, Y. Li, S. Wang, L. Wang, W. Chen *et al.*, “Lora: Low-rank adaptation of large language models.” *Iclr*, vol. 1, no. 2, p. 3, 2022.
- [28] Y. Lipman, R. T. Q. Chen, H. Ben-Hamu, M. Nickel, and M. Le, “Flow matching for generative modeling,” 2023. [Online]. Available: <https://arxiv.org/abs/2210.02747>
- [29] K. Kuckreja, M. S. Danish, M. Naseer, A. Das, S. Khan, and F. S. Khan, “Geochat: Grounded large vision-language model for remote sensing,” in *Proceedings of the IEEE/CVF conference on computer vision and pattern recognition*, 2024, pp. 27 831–27 840.
- [30] J. Bai, S. Bai, S. Yang, S. Wang, S. Tan, P. Wang, J. Lin, C. Zhou, and J. Zhou, “Qwen-vl: A versatile vision-language model for understanding, localization, text reading, and more,” *arXiv preprint arXiv:2308.12966*, 2023.
- [31] A. Singh, A. Fry, A. Perelman, A. Tart, A. Ganesh, A. El-Kishky, A. McLaughlin, A. Low, A. Ostrow, A. Ananthram *et al.*, “Openai gpt-5 system card,” *arXiv preprint arXiv:2601.03267*, 2025.
- [32] J. Hessel, A. Holtzman, M. Forbes, R. Le Bras, and Y. Choi, “Clipscore: A reference-free evaluation metric for image captioning,” in *Proceedings of the 2021 conference on empirical methods in natural language processing*, 2021, pp. 7514–7528.
- [33] C. Schuhmann, R. Beaumont, R. Vencu, C. Gordon, R. Wightman, M. Cherti, T. Coombes, A. Katta, C. Mullis, M. Wortsman *et al.*, “Laion-5b: An open large-scale dataset for training next generation image-text models,” *Advances in neural information processing systems*, vol. 35, pp. 25 278–25 294, 2022.
- [34] X. Wu, Y. Hao, K. Sun, Y. Chen, F. Zhu, R. Zhao, and H. Li, “Human preference score v2: A solid benchmark for evaluating human preferences of text-to-image synthesis,” *arXiv preprint arXiv:2306.09341*, 2023.